Pure Appl. Geophys.

DOI 10.1007/s00024-014-0983-8

Pure and Applied Geophysics

Deep-Water Characteristics of the Trans-Pacific Tsunami from the 1 April 2014 M_w 8.2 Iquique, Chile Earthquake

Mohammad Heidarzadeh,[1] Kenji Satake,[1] Satoko Murotani,[1] Aditya Riadi Gusman,[1] and Shingo Watada[1]

Abstract—We studied the tsunami generated by the 1 April 2014 M_w 8.2 Iquique (Chile) earthquake using 20 Deep-ocean Assessment and Reporting of Tsunamis (DART) records and applying Fourier and wavelet analyses as well as performing numerical simulations. Deep-water tsunami wave heights were in the range of 0.8–35.0 cm. For the stations located more than 2,200 km from the source, the average wave height was 1.7 ± 1.1 cm. The observed tsunami arrivals were delayed by 1–17 min relative to the simulated ones based on the linear long wave equations, and the delays were proportional to the tsunami travel distances. A small initial depression was observed at DART stations located at distances >10,000 km from the source whereas, traditionally, an initial elevation is expected at stations located seaward of subduction zones. Fourier analyses showed tsunami governing periods of 21.1 ± 1.7 and 14.7 ± 0.7 min, corresponding to a fault length of 60–70 km and a fault width of 40–45 km. While the two 21-min and 15-min signals appeared in most DART stations during ~0.5 h following the conventional arrival times, the 15-min signal was delayed at some far-field stations. Distribution of maximum DART wave heights across the Pacific Ocean did not show a meaningful relation between maximum DART wave heights and directivity or distance from the source.

Key words: Pacific Ocean, tsunami, Iquique earthquake of 1 April 2014, chilean tsunami, DART buoy, deep-water waves, fourier analysis, wavelet analysis, numerical modeling.

1. Introduction

A trans-oceanic tsunami was observed across the Pacific Ocean following the M_w 8.2 (USGS 2014) off Iquique (Chile) earthquake of 1 April 2014. The epicenter was at 19.610°S and 70.776°W (Fig. 1), with a depth of around 25 km and the origin time at 23:46:47 UTC (USGS 2014). The earthquake caused a death toll of at least seven in Chile and left over 200 injured (IOC-ITIC 2014). No fatality was reported due to the tsunami although some damage to coastal areas was reported. According to the Pacific Tsunami Warning Center (PTWC 2014), the tsunami waves reached almost all coastal areas within the Pacific Ocean registering maximum trough-to-crest tide gauge wave heights of: 4.25 m in Iquique (Chile), 1.17 m in Matarani (Peru), 0.32 m in Salina Cruz (Mexico), 1.09 m in Hiva Oa (French Polynesia), 0.33 m in Crescent City (California, USA), 1.13 m in Hilo (Hawaii, USA), 0.61 m in Waitangi (New Zealand), 0.71 m in American Samoa, 0.4 m in Vanuatu, and 0.34 m in Hakodate (Japan) (see Fig. 1 for locations).

The tsunami waves were also recorded on Deep-ocean Assessment and Reporting of Tsunamis stations (DART) across the Pacific Ocean. Development and deployment of DART buoys in world's oceans in recent years have provided an opportunity to obtain refined information about tsunami sources and to better understand deep-water characteristics of tsunami propagation, in addition to its primary function as a vital part of tsunami warning systems. In this context, DART records of tsunamis have been efficiently used in tsunami research. Rabinovich *et al.* (2013a) studied open ocean energy decay of tsunamis by analyzing DART records of some recent trans-Pacific tsunamis. Okal *et al.* (2014) applied DART records of Pacific tsunamis along with other simulated ones to develop a formula relating earthquake size to far-field tsunami amplitude. Heidarzadeh and Satake (2013a) studied the source spectra of the 11 March 2011 Tohoku tsunami through its DART records. Watada *et al.* (2014) employed DART waveforms of recent tsunamis to explain arrival time delays

[1] Earthquake Research Institute (ERI), The University of Tokyo, 1-1-1 Yayoi, Bunkyo-ku, Tokyo 113-0032, Japan. E-mail: mheidar@eri.u-tokyo.ac.jp

Published online: 25 November 2014

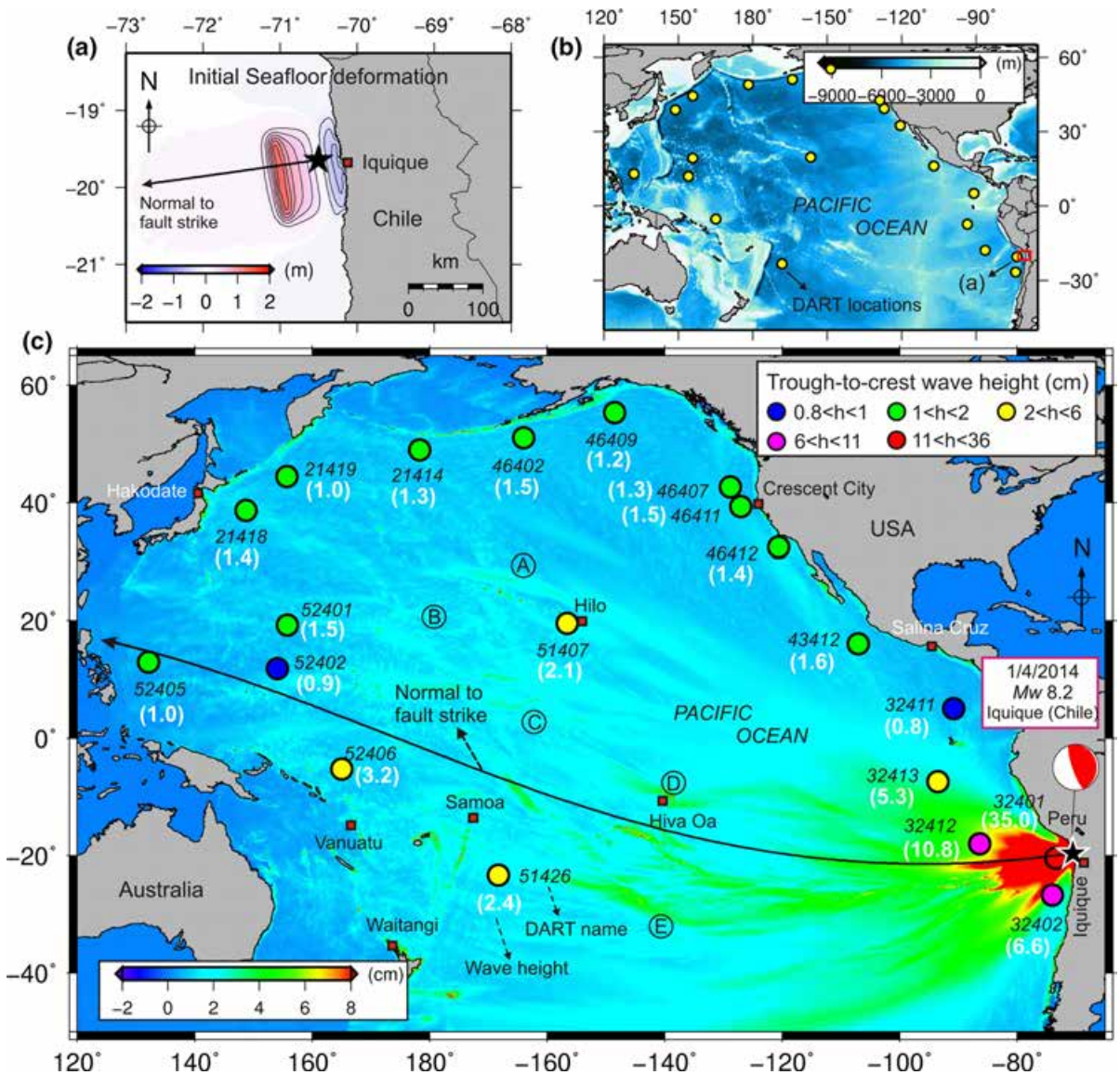

Figure 1

a Initial seafloor deformation due to the 1 April 2014 Iquique (Chile) earthquake based on our fault model (see Sect. 2.3). The *asterisk* shows the epicenter. **b** Bathymetry of the Pacific Ocean. The *small red rectangle* shows the location of **a**. The *yellow circles* are the locations of the DART stations used in this study. **c** Location of the epicenter (*black star*) and distribution of maximum trough-to-crest wave heights recorded on each DART station (*circles*) for the 2014 Iquique (Chile) tsunami. The *color map* shows distribution of the maximum tsunami amplitudes in each grid point during the entire Pacific-wide tsunami simulations. *Black and white numbers* are DART names and maximum trough-to-crest wave heights (in cm) for each DART station, respectively. The *solid black arrow* represents the normal direction to the fault strike. *Small filled rectangles* show some major cities. Characters *A–E* show locations with large wave amplitudes that are not located normal to the fault strike

and initial phase reversal relative to simulated tsunamis in the far-field. Here we study open-ocean characteristics of the 2014 off Iquique (Chile) tsunami by analyzing 20 DART records (Fig. 1). Main targets are: tsunami source periods, distribution of tsunami energy over time and frequency domains, and deep-water tsunami wave heights and their distribution within the Pacific Basin.

2. Data and Methodology

The data used in this study include 20 DART records with sampling intervals of 1 min provided by the US National Oceanic and Atmospheric Administration (NOAA 2014) (Table 1; Fig. 1). The water depth at the DART locations is in the range of 1,826–5,895 m indicating that only deep-water characteristics of the 2014 Iquique tsunami can be studied with such a dataset. Our methodology is a combination of statistical and spectral analyses of the observed tsunami waveforms along with numerical modeling. In the following, each method is briefly explained.

2.1. Waveform Preparation

The original DART data are provided with different sampling intervals of 15 s, 1 min, and 15 min. As discussed by Rabinovich *et al.* (2013a), during a tsunami event, the buoys are switched from the 15-min mode to the 15-s mode for several minutes and then transmit 1-min data until the end of the event. Switching between different

Table 1

The DART stations used to study the April 2014 Iquique tsunami along with characteristics of the tsunami waveforms

DART station	Location		Depth (m)	Dist. (km)[a]	Az. (°)[a]	TT (hh:mm)[b]	h (cm)[c]	$h_{5,000}$ (cm)[d]	Governing periods (min)	h_{sim} (cm)[f]	Initial polarity[g]
	Lon. (°E)	Lat. (°N)									
21414	178.26	48.95	5,375	13,160	315.66	17:47	1.3	1.3	21.6, 15.1	1.4	NA[h]
21418	148.77	38.69	5,662	15,679	307.69	20:28	1.4	1.4	21.6, 13.7	1.5	NA
21419	155.74	44.46	5,318	14,932	313.50	19:43	1.0	1.0	18.9, 15.1	1.1	NA
32401	−73.43	−20.47	4,865	288	251.02	0:18	35.0	34.8	21.6, 16.2	32.8	(+)
32402	−73.98	−26.74	4,070	853	201.79	0:58	6.6	6.3	21.6, 13.7	6.2	(+)
32411	−90.84	05.01	3,277	3,510	319.15	5:17	0.8	0.7	21.6, 15.1	0.7	NA
32412	−86.34	−17.98	4,387	1,644	273.87	2:07	10.8	10.5	21.6, 15.1	11.0	(+)
32413	−93.50	−7.40	3,890	2,800	295.83	3:40	5.3	5.0	21.6, 15.1	6.0	(+)
43412	−107.00	16.07	3,235	5,606	312.42	8:08	1.6	1.4	21.6, 13.7	1.8	NA
46402	−164.02	51.07	4,760	11,916	318.80	16:36	1.5	1.5	18.9, 15.1	1.4	(−)
46407	−128.81	42.67	3,322	9,120	320.81	13:26	1.3	1.2	19.8, 14.1	1.4	(−)
46409	−148.52	55.30	4,200	11,048	325.53	16:10	1.2	1.1	21.6, 15.1	1.3	(−)
46411	−127.02	39.35	4,259	8,779	318.93	12:52	1.5	1.4	19.0, 14.8	1.7	(+)
46412	−120.57	32.46	3,770	7,847	316.75	11:36	1.4	1.3	21.6, 15.1	1.8	NA
51407	−156.59	19.59	4,737	10,311	289.74	13:57	2.1	2.1	21.6, 15.1	1.8	(−)
51426	−168.29	−23.30	5,659	9,880	245.75	13:39	2.4	2.5	18.9, 13.7	2.7	(−)
52401	155.77	19.26	5,578	15,151	277.64	20:26	1.5	1.5	25.2, 13.7	2.1	NA
52402	154.04	11.87	5,875	15,156	266.75	20:20	0.9	0.9	30.2, 18.9, 13.7	1.4	NA
52405	132.18	12.99	5,895	17,459	256.80	23:45	1.0	1.0	24.2, 18.1, 14.5	0.8	NA
52406	165.00	−05.29	1,826	13,317	251.65	18:37	3.2	2.5	18.9, 15.1, 10.8	2.8	NA
Average and standard deviations							1.7 ± 1.1[e]		21.1 ± 1.7, 14.7 ± 0.7[i]	1.8 ± 1.2[e]	

[a] Distance (Dist.) and Azimuth (Az.) of every DART station to the epicenter are based on an spherical earth system

[b] Tsunami travel time (hour:min)

[c] h is the observed maximum trough-to-crest wave height

[d] Normalized wave heights at a water depth of 5,000 m using Green's law: $h_{5,000} = h\left(\frac{d}{5,000}\right)^{1/4}$, where h is the observed wave height, and d is the water depth at the location of DART stations in meters

[e] Without considering near-field stations with distances <20° (~2,200 km)

[f] Simulated maximum trough-to-crest wave height

[g] Either initial elevation (+) or depression (−)

[h] Not applicable

[i] For calculating the average values, the periods from DART-52402 were excluded

sampling modes is problematic causing some gaps and spikes as well as producing some repeating data points. Careful data processing of the original data was performed by removing gaps, spikes, and repeating values, and by making sure that the sampling interval is 1 min for the entire record. The data length varies from around 5 h to 12 h. Two different methods were used for de-tiding: (1) estimating tidal signals by polynomial fitting and then removing them from the original records and (2) high-pass filtering. For polynomial fittings, a polynomial of degree 10 was used for which we applied the function "*polyfit*" in the Matlab program (MATHWORKS 2014). For high-pass filtering, the "*Butterworth IIR*" digital filter from the Matlab signal processing toolbox is employed for which a cutoff frequency of 0.0002–0.0003 Hz (about 1–1.5 h) was chosen (MATHWORKS 2014). The reason for using two different methods was to make sure that our de-tiding process is sound. Figure 2 shows examples of de-tiding of the original records of three DARTs using the two methods mentioned above, indicating that the resulting de-tided waveforms from them are similar. We did not apply harmonic analysis for tidal predictions because such an analysis was not fruitful due to the short lengths of the 1-min DART data.

2.2. *Fourier and Wavelet Analyses*

Fourier analysis was performed using the fast Fourier transform (FFT) method for which the "*FFT*" function in Matlab program was used (MATHWORKS 2014; Heidarzadeh and Satake 2014b). Only the first 2.5 h of the tsunami waveforms were used for Fourier analysis in order to prevent reflected waves from appearing in our spectral analysis. Usually, tsunami waveforms at DART stations are free from local/regional bathymetric effects; however, in a Pacific-wide scale, still some reflected waves and regional bathymetric effects may be present in the recorded waveforms because many islands, seamount chains, and submarine ridges exist within the Pacific Ocean.

Since a tsunami is a non-stationary phenomenon, i.e., its spectral content varies with time, application of wavelet analysis is useful to better understand its behavior. Phenomena such as wave scattering, reflection, refraction, and dispersion can be studied by wavelet analysis, which treats tsunami waveforms both in time and frequency domains (Rabinovich and Thomson 2007; Heidarzadeh and Satake 2013a, b, 2014a; Borrero and Greer 2013). For wavelet analysis, we applied the wavelet package by Torrence and Compo (1998) using the "*Morlet*" mother function with a wavenumber of 6 and a wavelet scale width of 0.10.

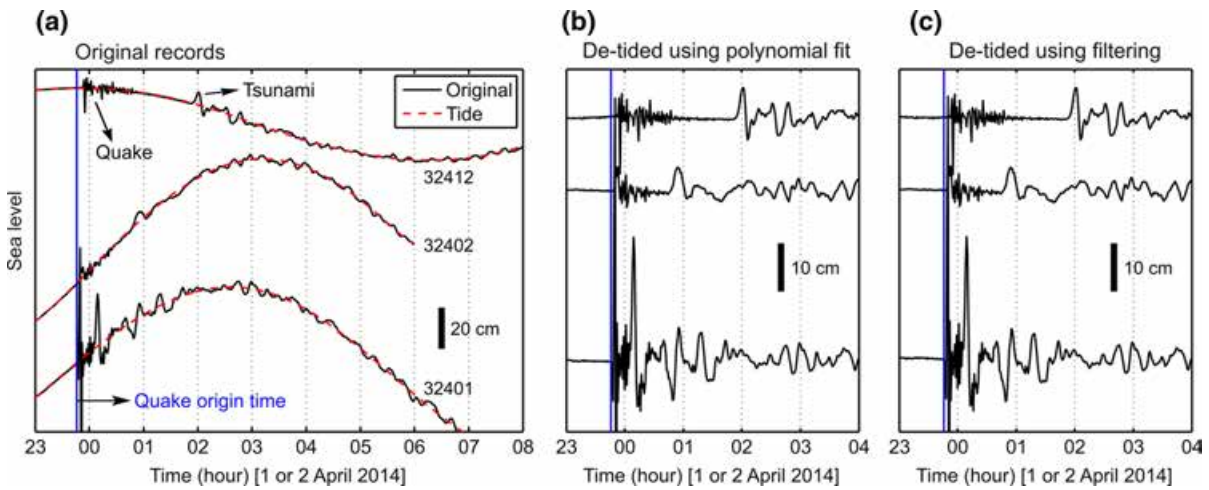

Figure 2
a Original records along with tide predictions using polynomial fittings. **b** De-tided waveforms by subtracting the predicted tidal signals from the original records. **c** De-tided waveforms using high-pass filtering

2.3. Numerical Modeling

We performed basin-wide tsunami simulations using a linear shallow water numerical model on a spherical coordinate system (model COMCOT, Liu *et al.* 1998). A 5-min bathymetric grid resampled from the 1-min GEBCO bathymetry grid (IOC *et al.* 2003) was used (Fig. 1). The time step for numerical modeling was 6.0 s, and simulations were conducted for a total time of 28.0 h. For tsunami simulations, we used a single rectangular fault with parameters of length 120 km, width 80 km, uniform slip 3.35 m, depth 10 km, strike 351°, dip 12°, and rake 91°. These source parameters were a combination of those reported by USGS (2014) and those obtained by our own source analysis (Gusman *et al.* 2014). As our purpose is to understand deep-water wave characteristics, not the source heterogeneity, we assumed a single fault with uniform slip. Before finalizing the fault parameters, a sensitivity analysis was performed by changing the slip amount in the range 3–5 m in order to reach the best slip value to reproduce the observed waveforms. Simulated tsunami waveforms were recorded at the location of each DART station.

3. Tsunami Waveforms and Their Properties

The results of de-tiding of 20 DART records using polynomial fits and high-pass filters were the same (Fig. 2); except for DARTs 32413, 52401, and 52405. We applied the former method for de-tiding in our study except in the aforesaid stations where the results of the latter method were adopted (Fig. 3). The tsunami signal was observed in all of the DART records indicating the trans-oceanic nature of the tsunami. The observed tsunami arrivals were delayed by 1–17 min relative to the simulated ones depending on the locations of the stations (Fig. 3). The travel time differences between observations and linear shallow-water simulations, based on a visual pick of the first positive peaks, are shown at the bottom-right corners of the panels (Fig. 3). The arrival time delays of the observed waves relative to the simulated ones in the far-field were attributed to the elastic loading of tsunamis, compressibility of sea water, and geopotential variations associated with the motion of mass during tsunami propagation as these effects are not included in the numerical simulations (Watada *et al.* 2014). Despite the arrival delays, the simulated and observed waveforms agree well in terms of amplitudes and periods. Such a good agreement using a single fault with uniform slip is not unusual because far-field tsunami propagation is not very much sensitive to the details of the tsunami source (Titov *et al.* 2005).

An unusual long-period initial wave was observed at DART 52401, which was also reproduced by simulations. A similar initial wave was seen in simulations at DART 52405, but it is hard to identify it in the observed record due to the high noise level (Fig. 3). These long initial waves are possibly the results of reflection/refraction/scattering of the tsunami within the western Pacific Ocean, which is heavily dominated by a wide range of bathymetric features and islands (e.g., Polynesian, Micronesian, and Melanesian Islands).

To better understand factors affecting the arrival time differences between the observed waveforms and the simulated ones based on the shallow water equations, we plotted these delays versus the distances of the DART stations from the source (Fig. 4a), versus the angles from the fault strike (Fig. 4b), versus the DART tsunami wave heights (Fig. 4c), and versus the combined effect of the distances and the angles (Fig. 4d). A clear positive correlation can be seen between the source distances and the arrival time delays (Fig. 4a). The largest arrival time delays appear to be concentrated around the normal direction to the fault strike (Fig. 4b, d). However, such a relationship is not strongly supported by our data. Just a few DART stations far from the epicenter happened to be located in the normal direction to the trench off the coast of Chile. In other words, the most important factor for the generation of these arrival delays is distance from the source. Almost no relationship can be seen between the deep-water wave heights and arrival time delays, at least for the 2014 Iquique tsunami (Fig. 4c).

3.1. Polarity of the Initial Phase

As for the polarity of the initial phase, it was not possible to identify the initial phase at some stations because the noise level was relatively high (Fig. 3).

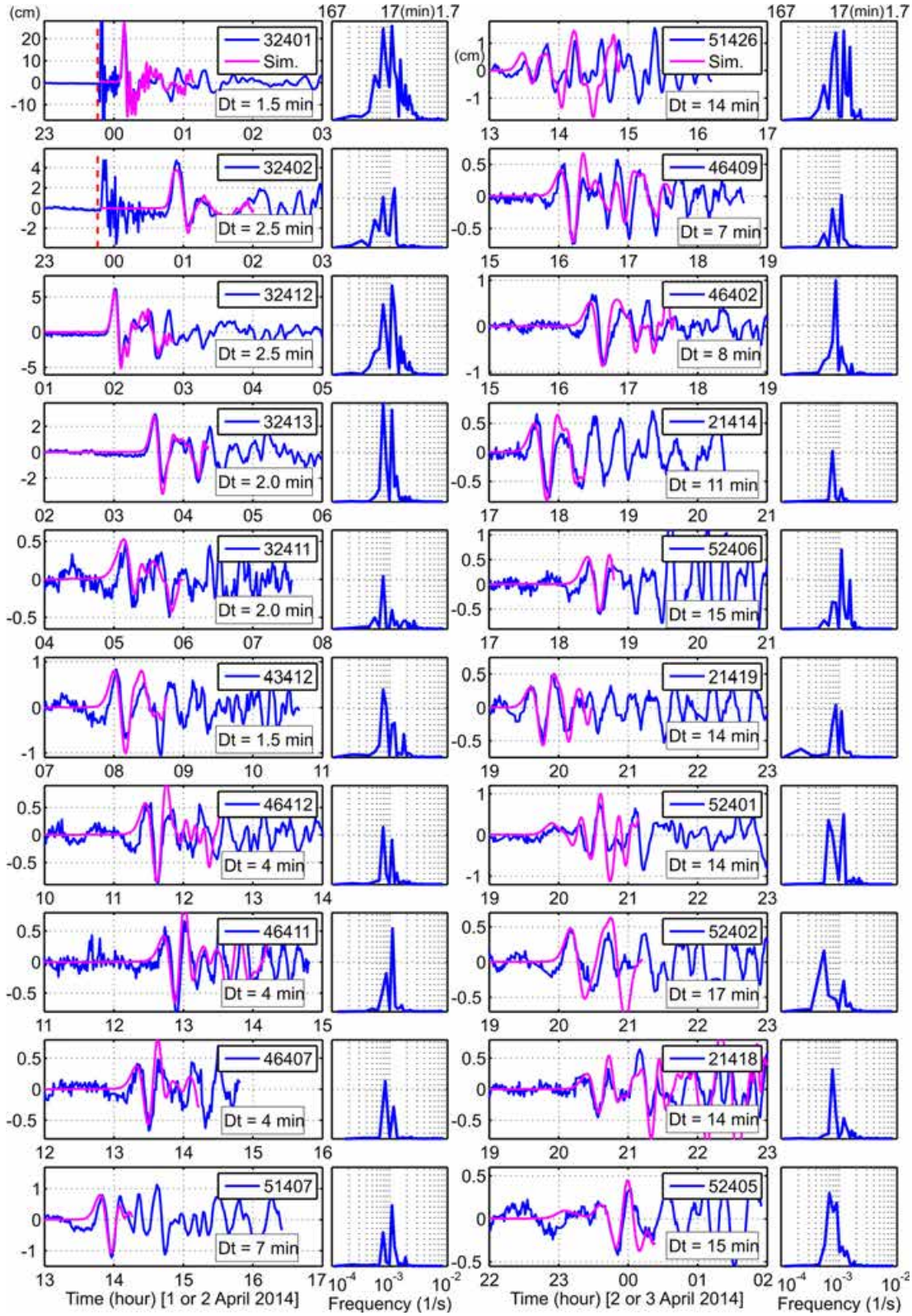
(cm)
32401
Sim.
Dt = 1.5 min
32402
Dt = 2.5 min
32412
Dt = 2.5 min
32413
Dt = 2.0 min
32411
Dt = 2.0 min
43412
Dt = 1.5 min
46412
Dt = 4 min
46411
Dt = 4 min
46407
Dt = 4 min
51407
Dt = 7 min
Time (hour) [1 or 2 April 2014]
167
17(min)1.7
Frequency (1/s)
51426
Sim.
Dt = 14 min
46409
Dt = 7 min
46402
Dt = 8 min
21414
Dt = 11 min
52406
Dt = 15 min
21419
Dt = 14 min
52401
Dt = 14 min
52402
Dt = 17 min
21418
Dt = 14 min
52405
Dt = 15 min
Time (hour) [2 or 3 April 2014]

◀ Figure 3
Tsunami waveforms (*thick-blue lines*) generated by the 1 April 2014 (Chile) earthquake along with respective spectra. *Thin-purple lines* represent simulated tsunami waveforms. The *red dashed-vertical line* represents the origin time of the earthquake. The *numbers in boxes at the bottom of the panels* are the time shifts applied to the simulated waveforms in order to match the observations. The values on vertical axes for the frequency plots are omitted because the absolute amounts of spectral energy are not important in this study. However, the amounts of spectral energy are given in Fig. 6

For stations with low noise level, we determined the polarity of the initial phase (Table 1). Classically, we expect an initial elevation in the seaward of subduction zones; however, the waveforms in Fig. 3 indicate an initial depression at stations located farther than 10,000 km from the source (Table 1). Although the first stages of the waveforms are not very clear, an initial depression cannot be overlooked, at least, at a few stations, e.g., DARTs 46407, 51407, and 46409. Phase reversal of tsunamis in the far-field has been reported by some authors (Okal 2011; Rabinovich *et al.* 2013b). According to Watada *et al.* (2014), this observed initial phase reversal at far-field DARTs is a characteristic response of the self-gravitating elastic Earth to tsunami loading, which causes reverse dispersion of long waves. According to this theory, if the initial phase at the tsunami source is positive seaward (e.g., for subduction thrust earthquakes), the recorded initial phase at far-field DARTs becomes negative. On the other hand, if the initial phase at the source is negative seaward (e.g., for normal-fault earthquakes), the recorded initial phase at far-field DARTs becomes positive.

3.2. *Distribution of Tsunami Energy in the Far-Field*

Distribution of maximum tsunami amplitudes by numerical modeling (Fig. 1c) shows that most of the tsunami energy is directed towards south and west of the Pacific Ocean, which can be attributed to the effect of tsunami directivity in the far-field.

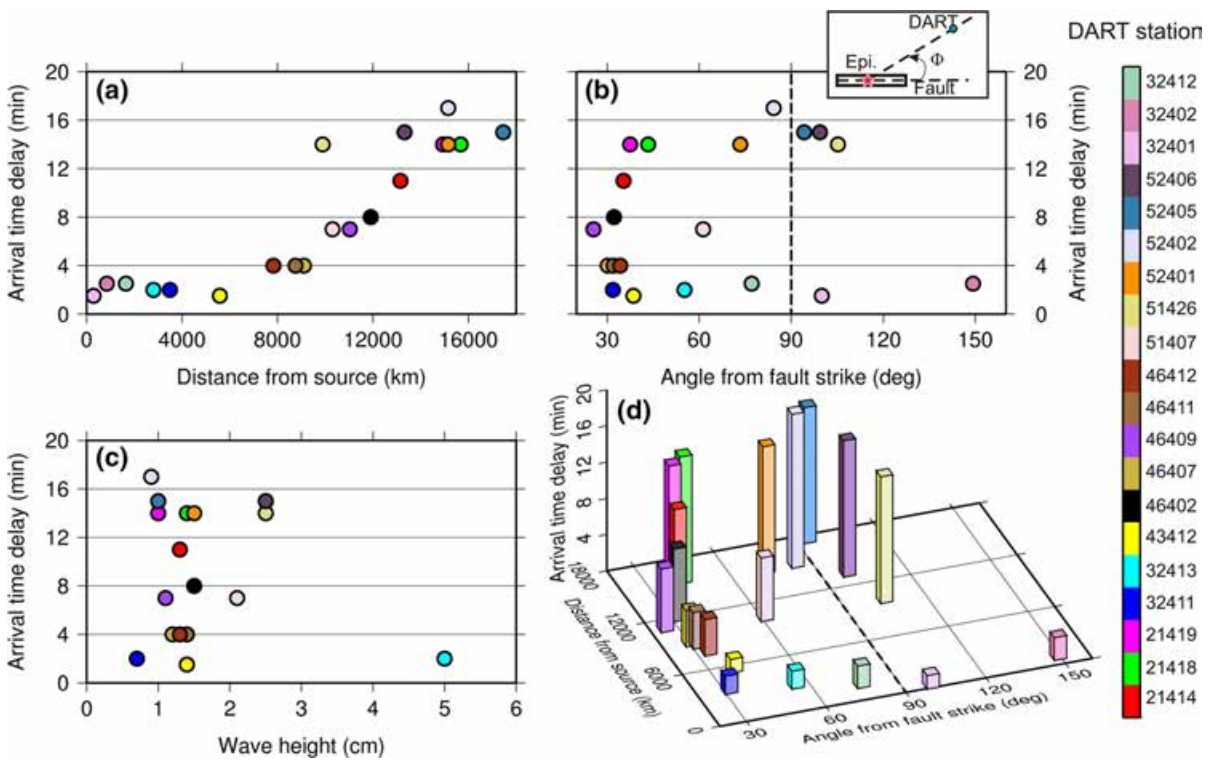

Figure 4
The arrival time delays of the observed waveforms relative to the simulated ones versus the distances from the source (**a**), versus the angles from the fault strike (angle Φ) (**b**), and versus the tsunami wave heights (**c**). **d** The combined effect of the distance and the angle from the fault strike on the arrival time delays

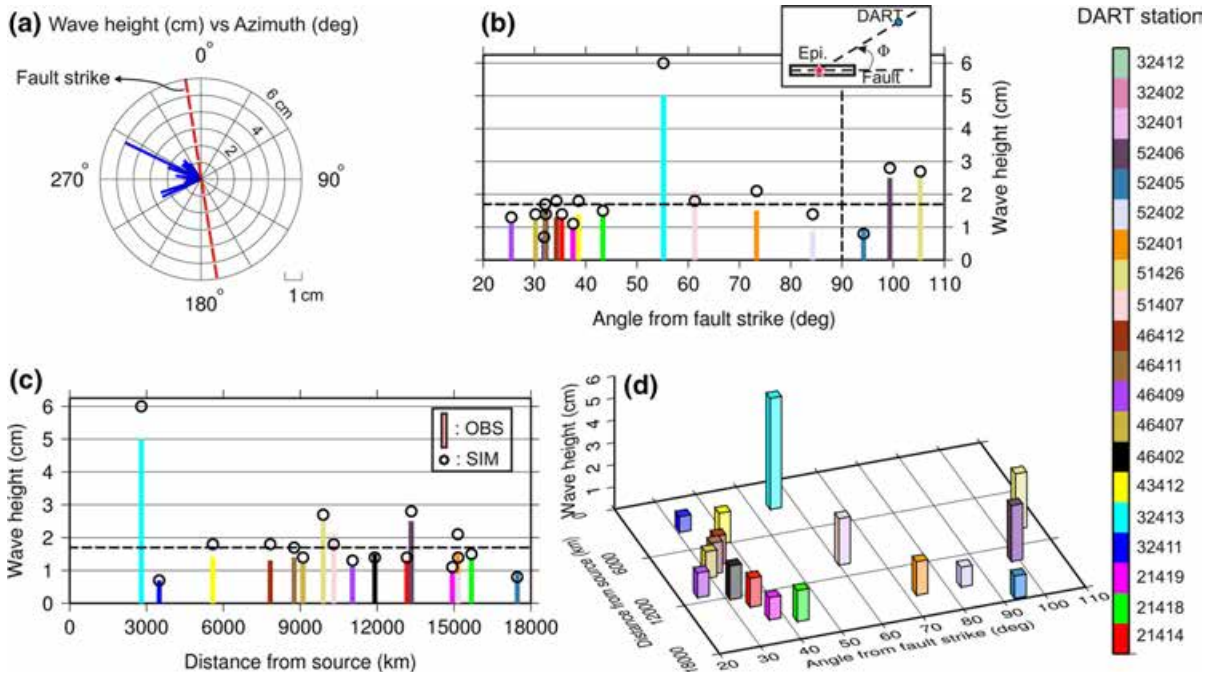

Figure 5

a Tsunami wave height at each DART station as a function of azimuth of each station. **b** Tsunami wave heights versus the angles from the fault strike. **c** Tsunami wave heights versus the distances of the DART stations from the source. The *horizontal dashed line* represents the average value of DART trough-to-crest wave heights. **d** Distribution of the maximum tsunami heights versus distances from the tsunami source and angles from the fault strike

According to the directivity of tsunami in the far-field of a thrust or normal fault (Ben-Menahem and Resenman 1972), the largest tsunami waves are expected at the normal direction to the fault strike. As the source fault is trending NNW–SSE (Fig. 1a), most of the tsunami energy is expected to travel in the SW direction according to the directivity effect (along the solid-black arrow in Fig. 1c). However, the effects of bathymetric features on tsunami energy distribution are also evident in Fig. 1c. Some of high-energy channels coincide with the locations of submarine seamount chains and ridges in the Pacific Basin (locations A–E in Fig. 1c). In fact, these bathymetric features act as waveguides (Satake 1988; Titov *et al.* 2005) or as scattering provinces (Mofjeld *et al.* 2001). The effect of seafloor bathymetry on far-field propagation of tsunamis was discussed by (Satake 1988). Four factors, i.e., directivity, refraction, reflection, and scattering, seem to affect far-field propagation of tsunamis in the Pacific Basin.

3.3. *Distribution of Maximum Deep-Water Wave Heights*

Among the analyzed stations, the maximum trough-to-crest tsunami height was recorded at the nearest station, i.e., DART 32401, with a value of 35.0 cm (Table 1; Fig. 1c). Except for the near-field DART stations (those located at the distances of <20°), the deep-water tsunami heights are in the range of 0.8–5.3 cm with an average value of 1.7 ± 1.1 cm (Table 1). Distribution of maximum wave heights in Fig. 1c may indicate that deep-water wave heights are not much sensitive to the distance of a DART station from the source or even to the directivity effect. To better examine this hypothesis, we plotted maximum deep-water wave heights versus azimuth (Fig. 5a), versus the angles of the DART stations from the fault strike (Fig. 5b), versus the distances from the source (Fig. 5c), and versus both effects together (Fig. 5d). To remove the effects of different water depths at the locations of DARTs on

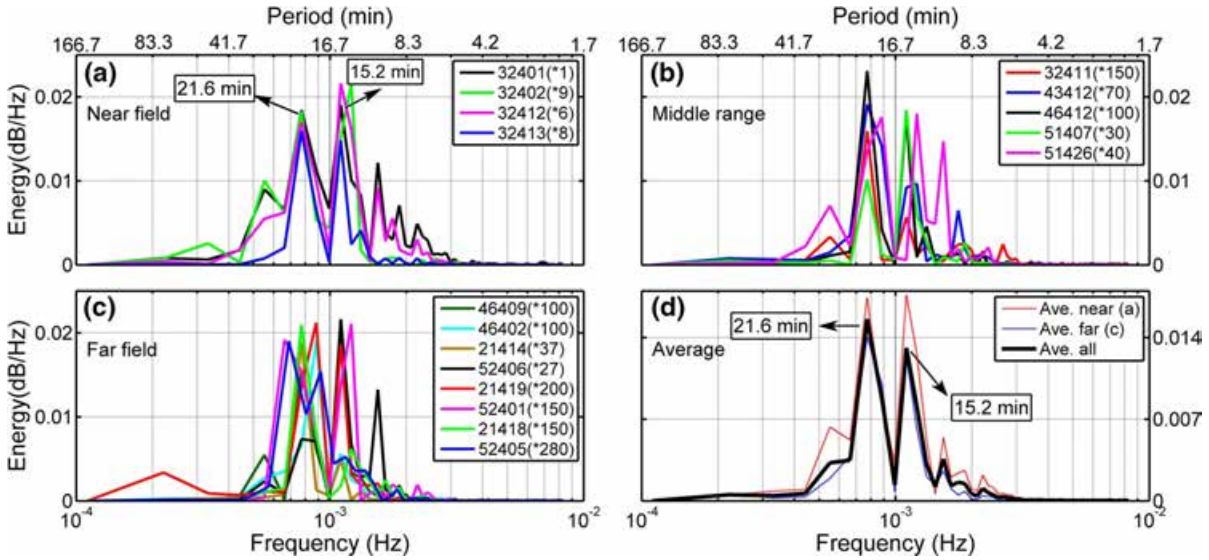

Figure 6
Comparison of the spectra of tsunami waveforms resulting from the 1 April 2014 Iquique earthquake recorded at DART stations in the near-field (**a**), in the middle range (**b**), and in the far-field (**c**). *Numbers in parentheses* are amplifying factors used to multiply the original spectra in order to facilitate their comparison. **d** Average spectra of the tsunami for the near-field (*red-thin line*; average of spectra in **a**), the far-field (*blue-thin line*; average of spectra in **c**), and all DART stations (*black-solid line*)

the recorded wave heights, we normalized the recorded heights to the water depth of 5,000 m using Green's law (Table 1). In an ideal case, we expect to see tsunami wave heights decreasing toward both sides of the right angle from the fault strike ($\Phi = 90°$ in Fig. 5b), and also decreasing by increasing the distance from the source up to 10,000 km (90°),and increasing again with the distance. Figure 5b–d does not show such trends. This is possibly because of the combined effect of the four factors of directivity, refraction, reflection, and scattering on far-field tsunami propagation. For example, although DART 52405 is located normal to the fault strike, it received a wave height of 1.0 cm which is among the minimum values recorded during this tsunami. This is because DART 52405 is located within the Philippines Sea where tsunami waves cannot penetrate easily due to the presence of numerous islands and seamount chains at its border.

4. Results of Fourier Analysis

The respective spectrum for each observed waveform is shown in Fig. 3. The spectra are relatively simple with two major peaks around 21 min and 15 min in most of the stations (Table 1). To better compare the spectra from different DART stations, they are overlaid in Fig. 6 for the near-field (Fig. 6a), the middle range (Fig. 6b), and the far-field stations (Fig. 6c). Because the level of spectral energy is different from station to station, we equalized the amounts of spectral energy by amplifying factors. It can be seen that the spectra from across the Pacific Ocean are similar to each other emphasizing the fact that they contain mostly tsunami source characteristics, and are almost free of non-tsunami sources (Rabinovich *et al.* 2013a). However, for stations far from the tsunami source, the spectra are slightly diverging from each other (Fig. 6c) although still the two major peaks at periods of ~21 min and ~15 min are clear.

Figure 6d presents averaged spectra for the near-field, the far-field, and all DART stations. The near-field average spectrum (Fig. 6d, red line) is similar to that of the far-field (Fig. 6d, blue line) implying that the DART records of this tsunami, even in the far-field, are free of non-tsunami sources. According to Table 1 and Fig. 6, the governing tsunami periods are: 21.1 ± 1.7 min and 14.7 ± 0.7 min. By assuming an average and constant water depth of around 1,000 m at the tsunami source, these governing periods imply a

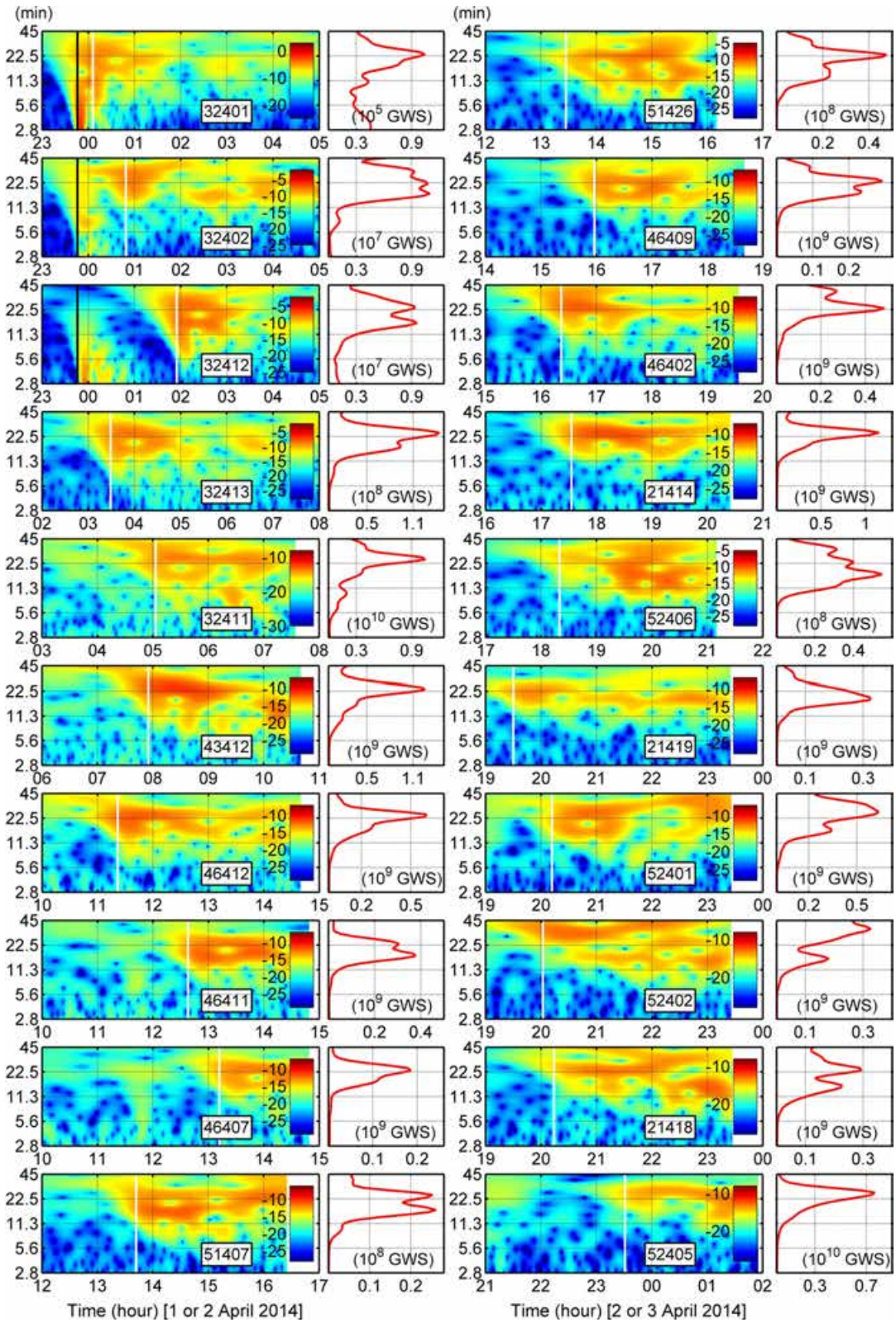
(min)
45
22.5
11.3
5.6
2.8
32401
(10^5 GWS)
32402
(10^7 GWS)
32412
(10^7 GWS)
32413
(10^8 GWS)
32411
(10^10 GWS)
43412
(10^9 GWS)
46412
(10^9 GWS)
46411
(10^9 GWS)
46407
(10^9 GWS)
51407
(10^8 GWS)
Time (hour) [1 or 2 April 2014]
51426
(10^8 GWS)
46409
(10^9 GWS)
46402
(10^9 GWS)
21414
(10^9 GWS)
52406
(10^8 GWS)
21419
(10^9 GWS)
52401
(10^9 GWS)
52402
(10^9 GWS)
21418
(10^9 GWS)
52405
(10^10 GWS)
Time (hour) [2 or 3 April 2014]

◀ Figure 7
Wavelet analysis for the DART records during the 1 April 2014 tsunami from the Iquique (Chile) earthquake. The *vertical black and white lines* represent the origin time of the earthquake and the conventional tsunami arrival times, respectively. Time-averaged wavelet spectrum over the time window is plotted to the right of each wavelet plot. *Vertical axes* for the spectra are the same as the wavelet plots. *GWS* stands for the global wavelet spectrum

source dimension of (60–70) km [length in strike direction] × (40–45) km [width in dip direction] for the tsunami source using the method described by Rabinovich and Thomson (2007). This estimate is close to the largest parts of the slip distribution by An *et al.* (2014), and Gusman *et al.* (2014) obtained by tsunami waveform inversion.

5. Results of Wavelet Analysis

Figure 7 presents the results of wavelet analysis. The white lines represent the tsunami arrival times of the first elevation phase which we designate here as the conventional arrival time. Wavelet plots show that at most stations, the longer wave components with periods >22 min arrive earlier than the shorter components. This is possibly due to the dispersion effect; waves with longer periods travel faster than the shorter ones. Such a normal dispersion is a characteristic feature of gravity waves in the ocean (deviation from long waves) and is not related to the elasticity of the earth, compressibility of seawater, or geopotential variations because these three effects generate reverse dispersion at very long periods (Watada et al. 2014).

In general, the wavelet plots (Fig. 7) show that the tsunami energy is concentrated in the period band of around 12–25 min and is relatively less scattered in comparison to that for tide gauge records of tsunamis (e.g., Rabinovich and Thomson 2007; Heidarzadeh and Satake 2014a). In other words, the period band of tsunami energy shown in Fig. 7 is relatively free from non-tsunami sources. As for the arrival times and temporal behavior of the two governing periods of around 21 min and 15 min, Fig. 7 shows that the two periods corresponding to the tsunami source appear at many stations during ~0.5 h following the conventional arrival times. However, at DARTs 52402, 21418, and 52405, the first stages of tsunami oscillations are dominated by the 21-min signal, and then the 15-min signal appears.

Switching of the tsunami governing period from one period to another at different times is observed. For example, at DART 32402, the period of around 21 min is governing at early stages of tsunami arrival; then the period of around 15 min is governing between 2:00 and 3:00 a.m.; later the two peak periods of ~21 min and ~15 min are of similar strength. Similar behavior can be seen more or less in other stations. This behavior is indicative of the non-stationary nature of tsunami waves.

6. Conclusions

The tsunami from the 1 April 2014 Iquique (Chile) was studied using waveforms recorded at 20 DART stations. The main findings are:

1. Deep-water tsunami wave heights were in the range 0.8–35.0 cm. For the stations located in the far-field, the average wave height was 1.7 ± 1.1 cm.
2. While traditionally an initial elevation phase is expected at stations located seaward of subduction zones, a small initial depression phase was observed at some DART stations.
3. Tsunami governing periods were 21.1 ± 1.7 min and 14.7 ± 0.7 min, corresponding to a fault length of 60–70 km and a fault width of 40–45 km.
4. According to the wavelet analysis, while the two 21-min and 15-min signals appeared in most DART stations during ~0.5 h following the conventional arrival times, the 15-min signal was delayed at some far-field stations.
5. Distribution of maximum DART wave heights across the Pacific Ocean showed that a meaningful relation between DART wave heights and directivity or distances from the source cannot be established, at least for this tsunami.

Acknowledgments

The sea level data used in this study were provided through the USA National Oceanographic and

Atmospheric Administration (NOAA). We thank Hiroshi Tsuruoka and Takeo Ishibe at the Earthquake Research Institute (ERI) for assisting in preparation of some figures. Several figures were drafted using the GMT software (Wessel and Smith 1991). We are sincerely grateful to Prof. Alexander Rabinovich, the editor, and two anonymous reviewers for comments that improved this article. This study is supported by the Japan Society for the Promotion of Science (JSPS).

References

An, C., I. Sepúlveda, and P. L.-F. Liu (2014). *Tsunami source and its validation of the 2014 Iquique, Chile Earthquake*, Geophys. Res. Lett., *41*:3988–3994, doi:10.1002/2014GL060567.

Ben-Menahem, A., and Rosenman, M. (1972). *Amplitude patterns of tsunami waves from submarine earthquakes*, J. Geophys. Res., *77*:3097–3128.

Borrero, J.C. and Greer, S.D. (2013). *Comparison of the 2010 Chile and 2010 Japan tsunamis in the Far-field*. Pure App. Geophys., *170* (6–8):1249–1274.

Gusman, A.R., Satake, K., Murotani, S., Heidarzadeh, M., Gunawan, E., Watada, S. (2014). *Rupture process of the 2014 Iquique Earthquake estimated from tsunami waveform and GPS data*. AGU Fall meeting 2014, Abstract No. S34B-02, December 15–19, San Francisco, USA.

Heidarzadeh, M., and Satake, K. (2013a). *Waveform and Spectral Analyses of the 2011 Japan Tsunami Records on Tide Gauge and DART Stations Across the Pacific Ocean*, Pure App. Geophys., *170* (6–8):1275–1293.

Heidarzadeh, M., and Satake, K., (2013b). *The 21 May 2003 Tsunami in the Western Mediterranean Sea: Statistical and Wavelet Analyses,* Pure App. Geophys., *170* (9–10):1449–1462.

Heidarzadeh, M., and Satake, K. (2014a). *The El Salvador and Philippines Tsunamis of August 2012: Insights from Sea Level Data Analysis and Numerical Modeling*, Pure App. Geophys., doi:10.1007/s00024-014-0790-2, pp 1–19.

Heidarzadeh, M., and Satake, K. (2014b). *Excitation of Basin-Wide Modes of the Pacific Ocean Following the March 2011 Tohoku Tsunami*, Pure App. Geophys., doi:10.1007/s00024-013-0731-5, pp 1–15.

IOC-ITIC (2014). *01 April 2014 (UTC), Mw 8.2, Northern Chile Tsunami*, available at: http://itic.ioc-unesco.org/index.php?option=com_content&view=article&id=1879:01-april-2014-utc-mw-8-2-northern-chile-tsunami&catid=2129&Itemid=2558, (page visited on May 09, 2014).

IOC, IHO, and BODC (2003). *Centenary edition of the GEBCO digital atlas*, published on CD-ROM on behalf of the Intergovernmental Oceanographic Commission and the International Hydrographic Organization as part of the general bathymetric chart of the oceans. British Oceanographic Data Centre, Liverpool, UK.

P. L.-F. Liu, Woo, S-B., and Cho, Y-S. (1998). *Computer programs for tsunami propagation and inundation*, Technical report, Cornell University, USA.

MATHWORKS (2014). MATLAB user manual, The Math Works Inc., MA, USA, 282 p.

Mofjeld, H.O., Titov, V.V., González, F.I., and Newman, J.C. (2001). *Tsunami scattering provinces in the Pacific Ocean,* Geophys. Res. Let., *28*(2):335–337.

NOAA (2014). *National Data Buoy Center-National Oceanic and Atmospheric Administration (NOAA) of USA*. http://www.ndbc.noaa.gov/dart.shtml (page visited on May 16, 2014).

Okal, E.A., Reymond, D., and Hébert, H. (2014). *From earthquake size to far-field tsunami amplitude: development of a simple formula and application to DART buoy data*, Geophys. J. Int., *196*(1):340–356.

Okal, E. A. (2011). *Tsunamigenic earthquakes: past and present milestones*, Pure App. Geophys., *168*(6–7):969–995.

PTWC (2014). Sea level observations of *01 April 2014 (UTC), Mw 8.2, Northern Chile Tsunami*, available at: http://itic.ioc-unesco.org/images/stories/list_of_tsunamis/2014/01apr2014_chile/01apr2014_sl_obs_PTWC_20140407.doc, (page visited on May 09, 2014).

Rabinovich, A.B., Candella, R.N., and Thomson, R.E. (2013a). *The open ocean energy decay of three recent trans-Pacific tsunamis,* Geophys. Res. Lett., *40*(12):3157–3162.

Rabinovich, A.B., Thomson, R.E., and Fine, I.V. (2013b). *The 2010 Chilean tsunami off the west coast of Canada and the northwest coast of the United States*, Pure App. Geophys., *170*(9–10):1529–1565.

Rabinovich, A.B., and Thomson, R.E. (2007). *The 26 December 2004 Sumatra tsunami: analysis of tide gauge data from the World Ocean Part 1. Indian Ocean and South Africa*, Pure Appl. Geophys., *164*:261–308.

Satake, K. (1988). *Effects of bathymetry on tsunami propagation: application of ray tracing to tsunamis,* Pure App. Geophys., *126* (1):27–36.

Titov, V., Rabinovich, A.B., Mofjeld, H.O., Thomson, R.E., and González, F.I. (2005). *The global reach of the 26 December 2004 Sumatra tsunami*, Science, *309*(5743):2045–2048.

Torrence, C., and Compo, G. (1998), *A Practical Guide to Wavelet Analysis*, Bull. Am. Met. Soc., *79*: 61–78.

USGS (2014). *US Geological Survey—Earthquake hazards program*, available at: http://comcat.cr.usgs.gov/earthquakes/eventpage/usc000nzvd#summary (page visited on May 09, 2014).

Watada, S., Kusumoto, S., and Satake, K. (2014). *Traveltime delay and initial phase reversal of distant tsunamis coupled with the self-gravitating elastic Earth*, J. Geophys. Res. doi:10.1002/2013JB010841.

Wessel, P. and Smith, W. H. F. (1991). *Free software helps map and display data*, EOS Trans. AGU *72*: 441.

(Received August 22, 2014, revised November 4, 2014, accepted November 5, 2014)